

Nonlinear Analysis of Axi-Symmetric Solid Using Vector Mechanics

T.Y. Wu¹

Abstract: In this work nonlinear analysis of axi-symmetric solid using vector mechanics is performed, in which a triangular solid unit developed in compliance with the concept of vector form analysis is proposed. The vector form analysis uses point value description (rather than function) to describe motion and configuration of solid, which has governing equation directly formulated with respect to each mass point (particle). The point value description includes particles allocation for configuration and defining path elements for particle motion. In addition, constitutive conditions are properly defined to complete the formulation. The constitutive conditions linking the mass points in deformable solids are primarily complemented by the generalized forces evaluated by a solid unit which is developed in a set of physical modeling procedures. Along each path element, particle motion is described by Newton's law of motion for free particles or by prescribed path for constrained particles. Implementations of vector form analysis presented herein are carried out employing the solution steps of vector form intrinsic finite element (VFIFE). Numerical examples with behaviors of large deformation, nonlinear material properties, and contact for benchmark verifications are performed to demonstrate the capability and accuracy of the approach developed under the framework of vector form analysis.

Keywords: vector mechanics, axi-symmetric solid, large deformation.

1 Introduction

Vector mechanics is the foundation of classical mechanics, in which particles are used to describe motion of objects subjected to natural forces. Directly using particles to describe motion of bodies and to solve practical structural problems possesses generality. However, in the days without computational tools, directly applying vector mechanics to engineering practice must face the challenges of

¹ Mechanical System Engineering Program, Institute of Nuclear Energy Research ROC AEC, Taiwan R.O.C.

considerable numbers of parameters, let alone complex particle interactions. The framework of analytical mechanics alleviates the problems encountered in vector mechanics. Rather than point values, functions are employed to describe the parameters required in kinematics and kinetics, and geometry. Based on the function parameters assumed or selected, governing equations of differential elements can be formulated in differential forms. Then, according to the characteristics of practical engineering problems, the governing equations can be further simplified and finally solved with the tools provided in analytical mathematics. The well-known example is that the problems with large overall motion are commonly treated by rigid body mechanics, but the stress or deformation is commonly handled by elasticity or mechanics of material.

For problems in engineering practice, formulating governing equation suitable for solving problems in practice is not an easy task to engineers. Even though the governing equation exists, analytical solutions may be limited to those with simple configuration and boundary conditions. With the advancement of computational technologies, mathematical procedures for analytical solutions have nearly been replaced by numerical approaches. Many well-known computational methods such as finite element methods, finite difference methods, boundary element methods, and meshless methods had been successfully developed, which in turn formed the modern computational mechanics [Atluri (2004); Atluri (2005)]. These numerical methods lead analytical mechanics to have extensive applications in engineering nowadays. Theoretical formulations and solution procedures, however, gradually branch into two inconsistent aspects. For instance, numerical methods for the solvers of analytical mechanics should obey the basic assumptions, such as the continuity in functions, originally made in formulations. These assumptions or simplifications may be helpful to the solution procedures in analytical mathematics. Nevertheless, they could also become obstacles to solutions in numerical approaches. In order to detour the limitations inherent in analytical mechanics, some approaches developed directly using physical modeling have been proposed, such as the discontinuous deformation analysis (DDA) by Shi (1988) and the discrete element method (DEM) by Cundall (1971).

To develop a mechanics framework different from those in the framework of continuum and analytical mechanics, and to find a theoretical basis suitable for modern computational analysis, Ting and his co-workers [Ting, Wang, Wu, Wang, and Chuang (2006); Ting, Duan and Wu (2008)] have conducted a series of researches on seeking a framework directly rooted in vector mechanics. In contrast to analytical mechanics, point value description is adopted.

The point value description is achieved by allocating mass particles for describing configuration, defining path elements for particle motion, and properly selecting

and using constitutive conditions to complete the formulation. Along each path element, the particle motion is described by Newton's law for the free particles or in a prescribed path for constrained particles. The constitutive conditions linking the particles in deformable solids are complemented by the generalized forces evaluated by the solid units developed in a set of physical modeling procedures, initially proposed by Ting, Shi and Wang (2004a, 2004b); Shi, Wang, and Ting (2004). It is the most crucial work in vector form analysis. Approximately in the last decade, several elements or units had been successfully developed and applied to the analyses of 2D frame structures [Ting, Shi and Wang (2004a); Wu, Wang and Wang (2006); Wu, Tsai and Lee (2009); Wu, Tsai and Lee (2010)], 3D membrane structures [Wu, Wang, Chuang and Ting (2007); Wu and Ting (2008)], 2D solids [Ting, Shi and Wang (2004a); Wu, Lee and Ting (2008)], and 3D solids [Wu and Ting (2004)]. The significance of using point value description is that both deformation and motion of structures or solids can be treated by a unified formulation. It is demonstrated by the numerical implementations and verifications presented in the works by [Wu and Ting (2004); Wu, Lee and Ting (2008)].

In this work, vector mechanics is used to analyze the multi-nonlinear problems of axisymmetric solid, in which the theory of vector form analysis is introduced. Under such a framework, a triangular solid unit for axisymmetric solid analysis is proposed. The remainder of this paper is organized as follows. Section 2 introduces the concept and theory of vector form analysis. Section 3 introduces VFIFE and the related solution procedures via a triangular solid unit. Section 4 briefly introduces the plasticity model used in this paper. In Section 5, numerical examples are illustrated to demonstrate the performance of vector form analysis on axisymmetric solid problems with multi-nonlinearity. Finally, in Section 6, conclusions are made.

2 Vector form analysis

The objective of vector form analysis is to build a framework of mechanics suitable for simulating structures with complex behaviors, such as large deformation, large overall motion, fragmentation, and so forth. Synthetically, it contains three fundamental concepts:

- (1) Point values of a set of spatial point are employed to describe the parameters for continua. The values of parameters between one particle and another are calculated by a set of canonical interpolation functions.
- (2) A set of point values of temporal points is used to describe the motion of spatial points. The process between any two temporal instants is calculated using a set of governing equations.

- (3) The motion of structures is described by a set of equation of motion, which requires computing the interaction forces (or internal forces) between spatial mass points. The internal forces only depend on pure deformations. In vector form analysis, a procedure of reverse motion is proposed to handle the calculation of pure deformations. More details are further introduced in Section 3.

2.1 Point value description

One basic assumption in classical mechanics is that a body is composed of infinite particles. Particle position is described by a set of differentiable continuous functions. Namely, there are infinite numbers of independent position variables in the body. In vector form analysis, a body can also consist of infinite numbers of points; however, only finite numbers of points are selected as independent variables. The positions among different points are computed by a set of canonical interpolation functions. These functions must satisfy the continuity condition in a physical sense.

In the physical point of view, the point value description can be regarded as a body that is composed of spatial points linked by a set of canonical units (or elements). The motion and configuration of a body are determined by the positions of the spatial points. The units are deformed following the moving points, thus where internal forces arise from, to make the body remain a body. The body configuration depends on the choice of interpolation functions. Therefore, the point value is an approximation of a real structure.

Figure 1 illustrates the difference between function description and point value description. **Figure 1** (a) shows the configurations of the solid $a - b - c - d$ before and after deformation, both of which are defined by a continuous vector function $U(x, y, t)$ with space and time independent variables. If the function description is adopted in formulation, other parameters, such as external forces, must also be written in terms of vector functions, $\mathbf{F}(x, y, t)$. The function description inevitably leads to the governing equation of problem has the form of partial differential equation. It is well-known that the solution of partial differential equation is not an easy task for complex problems.

In vector form analysis, a set of points are selected to describe the shape of body. **Figure** (b) shows the solid $a - b - c - d$ described by 16 points with position variables $(x_\alpha(t), y_\alpha(t))$ and external force vectors, $\mathbf{F}_\alpha(t)$, $\alpha = 1, \dots, 12$.

The advantage of using a finite number of points for description is that the point motion can be directly calculated in Newton's law. The conditions of loading, external forces and restraints can be described by point displacements and point forces. In short, Newtonian mechanics or vector mechanics can be directly employed and the barriers in analytical mechanics can be avoided. The equation of motion for a par-

ticle in Newtonian mechanics is ordinary differential equation with respect to time, but the equation of motion for a differential element in Euler-Cauchy continuum is partial differential equation with respect to space and time [Ting, Duan, and Wu (2011)].

2.2 Path element and governing equation

Another characteristic of vector form analysis is the employment of path element. In **Figure 2 (a)**, the motion trajectory of a particle j in a solid is illustrated. The trajectory consists of a set of segments identified by a series of time instants t_k , $k = 0, 1, 2, \dots, a, b, \dots, m$. The trajectory segment of $t_a \leq t \leq t_b$ is referred to as a path element of particle j when it lies between \mathbf{x}_{ja} and \mathbf{x}_{jb} , as shown in **Figure 2 (b)**. The behavior of particles in the path element $t_a \leq t \leq t_b$ is determined by the equations governed by Newton's 2nd law of motion, if particle j is in free motion:

$$m_j \ddot{\mathbf{x}}_j = \mathbf{F}_j + \mathbf{f}_j \quad t_a \leq t \leq t_b \quad (1)$$

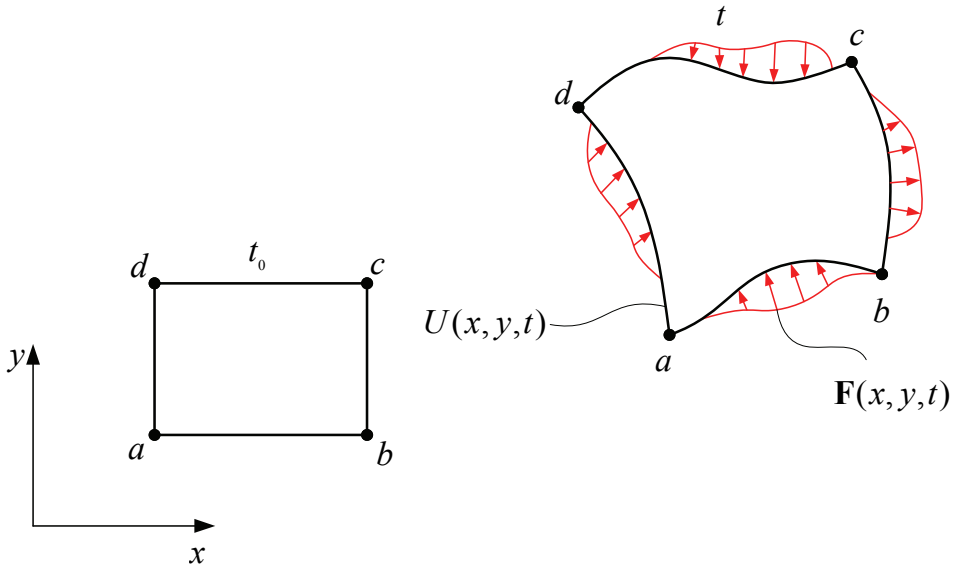
m_j , $\ddot{\mathbf{x}}_j$, and \mathbf{F}_j respectively denotes the mass, acceleration vector, and external force vector. In addition, \mathbf{f}_j represents the interaction forces with its neighboring particles. In vector form analysis, the interaction forces in deformable structures or solids are mainly supplemented by a series of VFIFE elements. For any solid, a patch consisting of several solid units is used to evaluate the interaction forces acting at a particle, as illustrated in **Figure 3**. The evaluation of interaction forces in axisymmetric solid using a triangular unit is demonstrated in Section 3.

The definition of path element facilitates the method developed under the framework of vector form analysis to treat fragmentation encountered in continua. Within a path element, both particle mass and interactions with neighboring particles are kept in constant. Fragmentations of solid or merging of particle are allowable only at the beginning or ending of each path element (t_a or t_b).

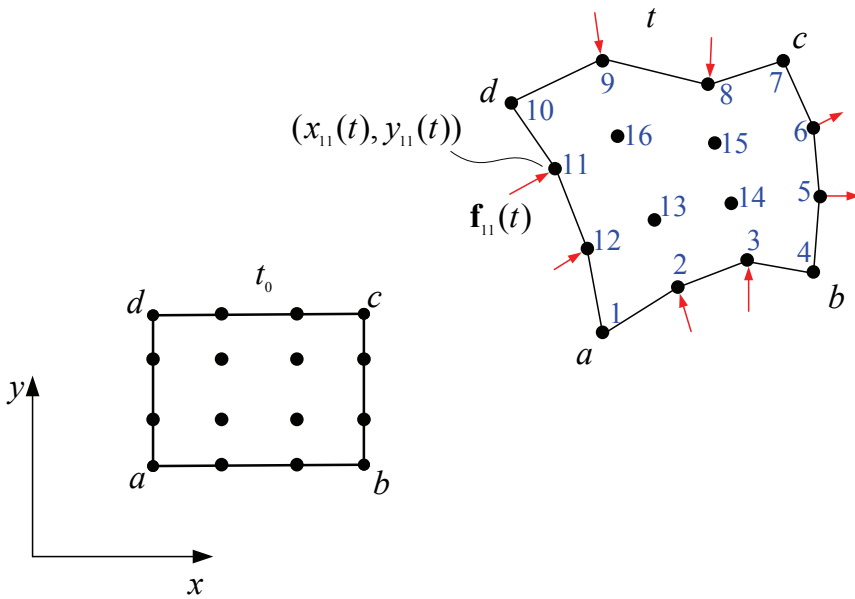
3 Particle interaction forces in axisymmetric solid

In vector form analysis, particle interaction forces in deformable solid are evaluated purely with physical modeling, rather than the result of variational principles. The basic idea is to treat a solid unit analog to a particle with finite size in continuum mechanics. Thus a body is a physical collection of all solid units. In this section, a triangular unit for axisymmetric solid is performed.

Figure 4 illustrates a solid shaped by a 2D area revolving about z -axis. The cylindrical global coordinate system (r, z, θ) is employed for convenience. If the applied forces and restraint conditions of the solid are also axisymmetric, the behavior of



(a)



(b)

Figure 1: Descriptions for continuum: (a) Function description for solid (b) Point value description for solid.

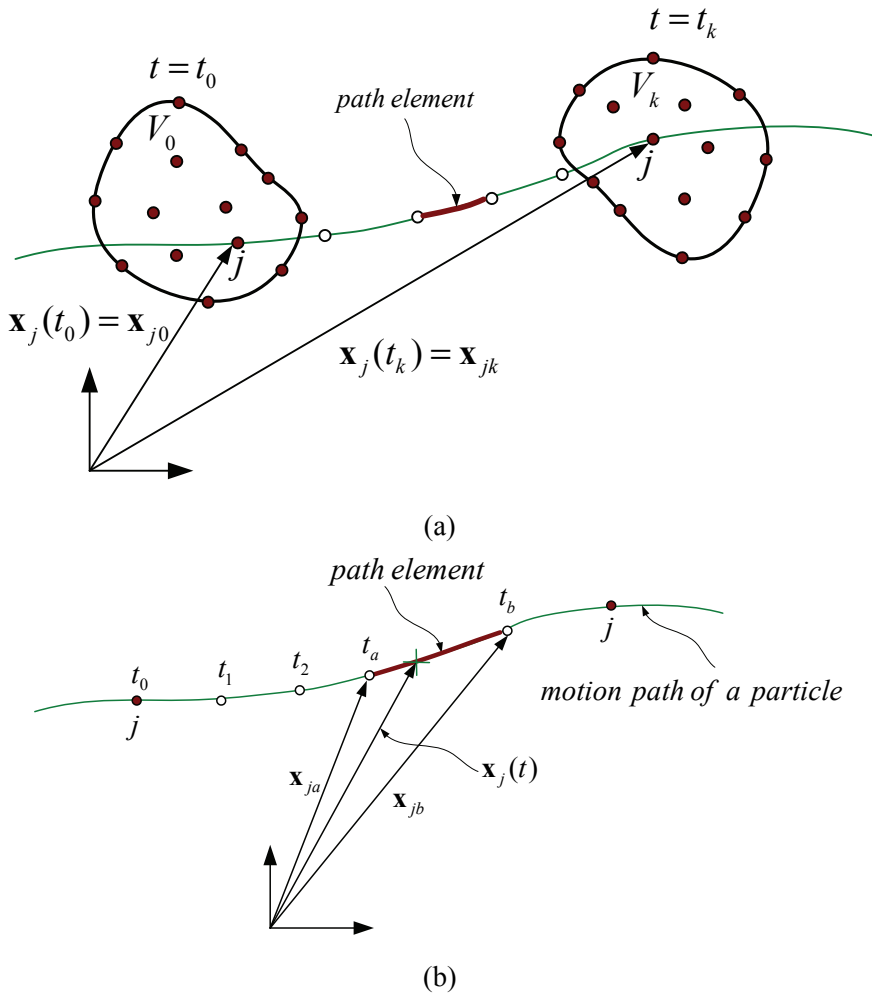


Figure 2: (a) Motion of particle j in a solid described by points. (b) Path element, $t_a \leq t \leq t_b$.

whole structure can be modeled by a finite number of particles moving on an arbitrary $r - z$ plane, as illustrated in **Figures 4** and **5**. The interaction forces of particle j with its neighbors are evaluated by the patch connecting it, as shown in **Figure 5**.

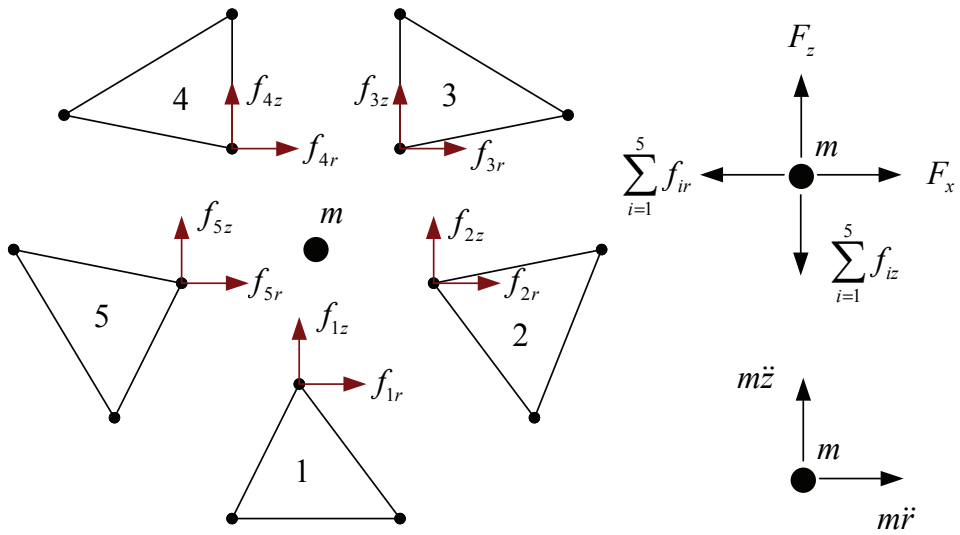


Figure 3: Solid units and free body of a particle.

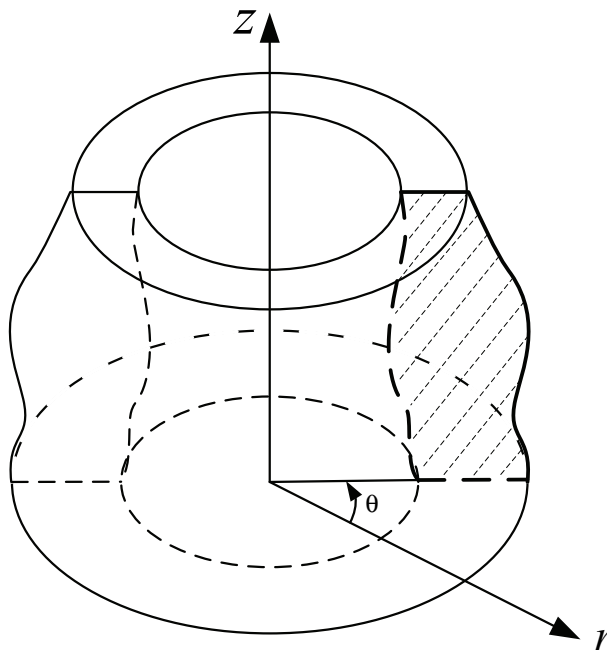


Figure 4: An axisymmetric solid with a symmetric axis z .

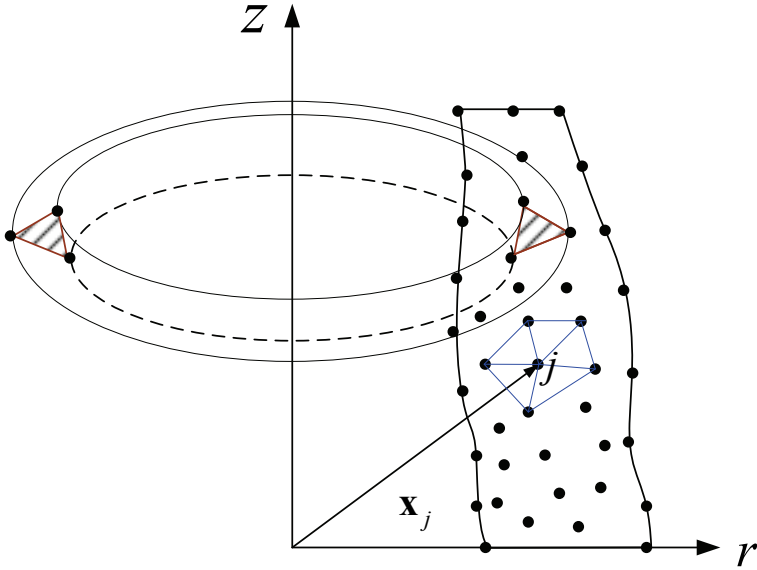


Figure 5: Point mass j and connecting patch.

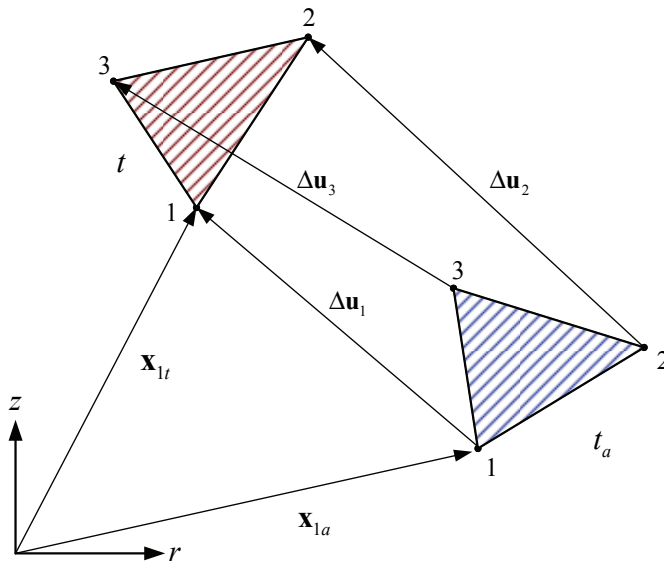


Figure 6: Motion states of a triangular solid unit.

3.1 Nodal deformation displacement

Figure 6 shows a triangular solid unit connecting 3 particles with nodal numbers (1, 2, 3) moving on the rz -plane. The configuration, nodal positions, stress, strain, and related material properties of the solid unit are given at time t_a . In addition, along the path element, $t_a \leq t \leq t_b$, material properties are kept in constant and configuration change can be neglected. At time t_a , the position and displacement vectors of node I is \mathbf{x}_{Ia} and \mathbf{u}_{Ia} , and at time t , \mathbf{x}_{It} and \mathbf{u}_{It} . Thus the displacement vector of node I from t_a to t is

$$\Delta \mathbf{u}_{It} = \mathbf{x}_{It} - \mathbf{x}_{Ia}, \quad I = 1, 2, 3 \quad (2)$$

The displacement increments in Eq. (2) contain rigid body motion and pure deformation. The rigid body motion does not induce any interaction forces, and thus it has to be eliminated. To do this, the solid unit is treated as a continuum particle with finite size. A fictitious reversed rigid body rotation is evaluated and then imposed on the solid unit to obtain nodal deformation vectors. The angle of rigid body rotation $\Delta\theta$ is calculated as follows,

$$\Delta\theta = \frac{1}{3} \sum_{I=1}^3 \Delta\phi_I \quad (3)$$

In which, $\Delta\phi_I$ denotes the rotation angle due to orientation change of node I to centroid C from t_a to t , as shown in **Figure 7**. It can be calculated by

$$\Delta\phi_I = \cos^{-1}(\mathbf{e}_{Ia} \cdot \mathbf{e}_{It}), \quad I = 1, 2, 3 \quad (4)$$

$$\mathbf{e}_{It} = \frac{\mathbf{x}_{It} - \mathbf{x}_{ct}}{\|\mathbf{x}_{It} - \mathbf{x}_{ct}\|}, \quad \mathbf{e}_{Ia} = \frac{\mathbf{x}_{Ia} - \mathbf{x}_{ca}}{\|\mathbf{x}_{Ia} - \mathbf{x}_{ca}\|}, \quad I = 1, 2, 3 \quad (5)$$

where \mathbf{x}_{ca} and \mathbf{x}_{ct} are the position vectors of centroid at time t_a and t .

It should be noted that the above calculation for the angle of rigid body rotation is merely a numerical measurement. It is to reduce the order of relative displacements contributed from rigid body rotation and then improve the accuracy of strain evaluation. With the rotation angle, the nodal displacement from rigid body rotation can be evaluated.

$$\Delta \boldsymbol{\eta}_I^r = (\mathbf{R}(-\Delta\theta) - \mathbf{I})\Delta \mathbf{x}_{It}, \quad I = 1, 2, 3 \quad (6)$$

where \mathbf{R} denotes the rotation matrix,

$$\mathbf{R}(\Delta\theta) = \begin{bmatrix} \cos(\Delta\theta) & -\sin(\Delta\theta) \\ \sin(\Delta\theta) & \cos(\Delta\theta) \end{bmatrix} \quad (7)$$

and \mathbf{I} is a 2×2 unity matrix. Therefore, the vector of nodal deformation displacement $\Delta \boldsymbol{\eta}_I^d$ is obtained.

$$\Delta \boldsymbol{\eta}_I^d = (\Delta \mathbf{u}_{It} - \Delta \mathbf{u}_{1t}) + \Delta \boldsymbol{\eta}_I^r, \quad I = 1, 2, 3 \tag{8}$$

The other significance of reverse rigid body motion is to make the calculations of stress and strain consistent along the path element. In other words, the configuration at time t_k is the referenced state of the solid unit.

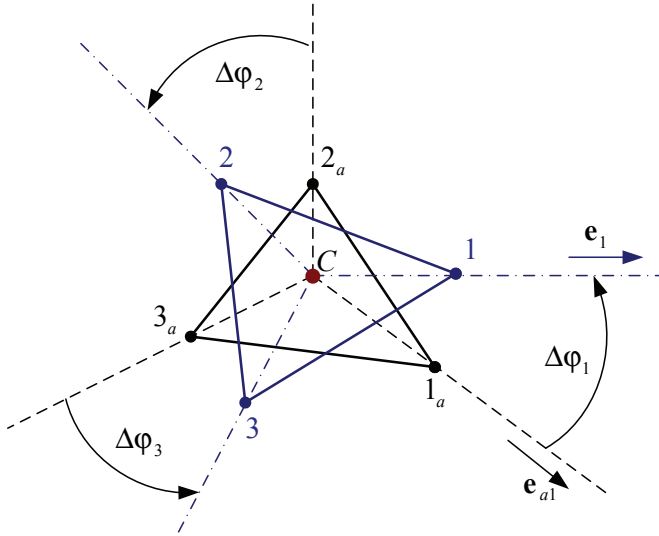


Figure 7: Rigid body rotation measured by rotation of orientations from node to centroid.

3.2 Deformation coordinate

Only three of the six deformation components in Eq. (11) are independent; therefore, three redundant DOFs' corresponding to rigid body modes must be eliminated. The elimination approach is by defining a set of coordinate system $\hat{x} = (\hat{r}, \hat{z})$, referred to as deformation coordinate, which can be determined by satisfying the following two conditions:

- The origin of the coordinate is located at node 1.
- In this coordinate system, the solid unit cannot contain rigid body rotation.

To satisfy condition 2, the \hat{r} -axis should parallel to the deformation vector of node 2, $\Delta\boldsymbol{\eta}_2^d$ and the orientation vector of the \hat{r} -axis, $\hat{\mathbf{e}}_1$, turns out to be

$$\hat{\mathbf{e}}_1 = \begin{Bmatrix} l_1 \\ m_1 \end{Bmatrix} = \frac{1}{|\Delta\boldsymbol{\eta}_2^d|} \begin{Bmatrix} \Delta\eta_{2r}^d \\ \Delta\eta_{2z}^d \end{Bmatrix} \quad (9a)$$

The coordinate transformation matrix is

$$\mathbf{Q} = \begin{bmatrix} l_1 & m_1 \\ -m_1 & l_1 \end{bmatrix} \quad (9b)$$

Thus, the relationship between deformation coordinate $\hat{\mathbf{x}}$ and global coordinate x can be written as

$$\hat{\mathbf{x}} = \mathbf{Q}(\mathbf{x} - \mathbf{x}_1) \quad (10)$$

For simplicity, what follows the variable with a hat, say $\hat{\boldsymbol{\lambda}}$, denotes that $\boldsymbol{\lambda}$ is expressed in a deformation coordinate system. It should be noted that the deformation vector of node 2 may be zero during computation. Under such situation it can be replaced by that of node 3 and, of course, some of algorithms discussed subsequently must be slightly modified.

3.3 Internal nodal forces

For convenience, the deformation components $\Delta\boldsymbol{\eta}_I^d$ are assembled in the vector form,

$$\mathbf{u}_d^T = \{\Delta\eta_1^d \quad \Delta\eta_2^d \quad \Delta\eta_3^d\} = \{u_1 \quad v_1 \quad u_2 \quad v_2 \quad u_3 \quad v_3\} \quad (11)$$

Let Eq. (14) be expressed in the deformation coordinate system,

$$\hat{\mathbf{u}}_d^T = \{\hat{u}_1 \quad \hat{v}_1 \quad \hat{u}_2 \quad \hat{v}_2 \quad \hat{u}_3 \quad \hat{v}_3\} \equiv \{0 \quad 0 \quad \hat{u}_2 \quad 0 \quad \hat{u}_3 \quad \hat{v}_3\} \quad (12)$$

where the three components, \hat{u}_1 , \hat{v}_1 and \hat{v}_2 are zero. It implies that three DOFs' are eliminated and the displacement vector $\hat{\mathbf{u}}_d$ now can be cast in a condensed form,

$$(\hat{\mathbf{u}}_d^*)^T = \{\hat{u}_2 \quad \hat{u}_3 \quad \hat{v}_3\} \quad (13)$$

Thus the definition of internal nodal forces can be written as,

$$\delta U = (\delta\mathbf{u}_d^*)^T \hat{\mathbf{f}}^* \quad (14a)$$

or expressed explicitly as

$$\delta U = \left\{ \delta \hat{u}_2 \quad \delta \hat{u}_3 \quad \delta \hat{v}_3 \right\} \begin{Bmatrix} \hat{f}_{2r} \\ \hat{f}_{3r} \\ \hat{f}_{3z} \end{Bmatrix} \quad (14b)$$

In the deformation coordinate, both internal nodal forces and nodal deformations are independent. For a constant strain triangular unit, the displacement increment at an arbitrary point (\hat{r}, \hat{z}) on the element from time t_a to t is denoted as $\hat{\mathbf{u}} = \{\hat{u}, \hat{v}\}^T$, which can be described by a set of shape functions, that is the same as that in the traditional finite element,

$$\begin{aligned} \hat{u} &= \hat{N}_2 \hat{u}_2 + \hat{N}_3 \hat{u}_3 \\ \hat{v} &= \hat{N}_3 \hat{v}_3 \end{aligned} \quad (15)$$

where \hat{N}_I , $I = 2, 3$ denotes the nodal shape functions in the deformation coordinate system. With the deformation shape functions, one can formulate the distributions of stress and strain within the element. If element deformations within time segment $t - t_a$ are infinitesimal, the relationship of the strain increment and the deformation displacements is

$$\Delta \hat{\boldsymbol{\varepsilon}}^* = \hat{\mathbf{B}} \hat{\mathbf{u}}_d^* \quad (16)$$

where

$$\Delta \hat{\boldsymbol{\varepsilon}}^* = \{\Delta \hat{\boldsymbol{\varepsilon}}_r \quad \Delta \hat{\boldsymbol{\varepsilon}}_z \quad 2\Delta \hat{\boldsymbol{\varepsilon}}_{rz}\}^T \quad (17)$$

$$\Delta \hat{\boldsymbol{\varepsilon}}_r = \frac{\partial \hat{u}}{\partial \hat{r}}, \quad \Delta \hat{\boldsymbol{\varepsilon}}_z = \frac{\partial \hat{v}}{\partial \hat{z}}, \quad \Delta \hat{\boldsymbol{\varepsilon}}_{rz} = \frac{1}{2} \left(\frac{\partial \hat{u}}{\partial \hat{z}} + \frac{\partial \hat{v}}{\partial \hat{r}} \right) \quad (18)$$

In addition, circumferential strain is calculated by

$$\Delta \hat{\boldsymbol{\varepsilon}}_\theta = \frac{\Delta \bar{u}}{\bar{r}} \quad (19)$$

where $\bar{r} = (r_{1t} + r_{2t} + r_{3t})/3$ and $\Delta \bar{u} = (\Delta u_{1t} + \Delta u_{2t} + \Delta u_{3t})/3$. Thus,

$$\Delta \hat{\boldsymbol{\varepsilon}} = \{\Delta \hat{\boldsymbol{\varepsilon}}^* \quad \Delta \hat{\boldsymbol{\varepsilon}}_\theta\} \quad (20)$$

The stress increment $\Delta \hat{\boldsymbol{\sigma}}$ can be obtained by the constitutive relationship of materials,

$$\Delta \hat{\boldsymbol{\sigma}} = D \Delta \hat{\boldsymbol{\varepsilon}} \quad (21)$$

where, matrix \mathbf{D} is the tangent modulus when the stress in solid unit is at time t_a , i.e. $\boldsymbol{\sigma}_a$.

$$\Delta \hat{\boldsymbol{\sigma}} = \{\Delta \hat{\boldsymbol{\sigma}}_r \quad \Delta \hat{\boldsymbol{\sigma}}_z \quad \Delta \hat{\boldsymbol{\tau}}_{rz} \quad \Delta \hat{\boldsymbol{\sigma}}_\theta\}^T = \{\Delta \hat{\boldsymbol{\sigma}}^* \quad \Delta \hat{\boldsymbol{\sigma}}_\theta\}^T \quad (22)$$

The internal virtual work of the solid unit can be written as

$$\delta U = \int_{V_a} (\delta \Delta \hat{\boldsymbol{\epsilon}}^*)^T \hat{\boldsymbol{\sigma}}^* dV_a = 2\pi \bar{r} \int_{A_a} (\delta \Delta \hat{\boldsymbol{\epsilon}}^*)^T (\hat{\boldsymbol{\sigma}}_a^* + \Delta \hat{\boldsymbol{\sigma}}^*) d\hat{A}_a \quad (23)$$

where V_a , A_a , and $\hat{\boldsymbol{\sigma}}_a$ respectively denote the volume, area of solid unit, and stress at time t_a . Therefore, Eq. (25) can be rewritten as

$$\delta U = (\delta \hat{\mathbf{u}}_d^*)^T \left[2\pi \bar{r} \int_{\hat{A}_a} \hat{\mathbf{B}}^T \hat{\boldsymbol{\sigma}}_a^* d\hat{A}_a + \left(2\pi \bar{r} \int_{\hat{A}_a} \hat{\mathbf{B}}^T \Delta \hat{\boldsymbol{\sigma}}^* d\hat{A}_a \right) \hat{\mathbf{u}}_d^* \right] \quad (24)$$

Comparing Eq. (17) with Eq. (26), the work equivalent nodal forces can be obtained,

$$\mathbf{f}^* = \mathbf{f}_a^* + \Delta \mathbf{f}^* \quad (25a)$$

$$\mathbf{f}_a^* = 2\pi \bar{r} \int_{\hat{A}_a} \hat{\mathbf{B}}^T \hat{\boldsymbol{\sigma}}_a^* d\hat{A}_a \quad (25b)$$

$$\Delta \mathbf{f}^* = \left[2\pi \bar{r} \int_{\hat{A}_a} \hat{\mathbf{B}}^T \Delta \hat{\boldsymbol{\sigma}}^* d\hat{A}_a \right] \hat{\mathbf{u}}_d^* \quad (25c)$$

In Eq. (27), only three forces components, $\{\hat{f}_{2r}, \hat{f}_{3r}, \hat{f}_{3z}\}$ are available. The remainder three can be obtained by three static equilibrium conditions on (\hat{r}, \hat{z}) plane, i.e.

$$\sum \hat{M}_\theta = 0, \quad \hat{f}_{2z} = (-\hat{f}_{2r}\hat{z}_2 + \hat{f}_{3r}\hat{z}_3 - \hat{f}_{3z}\hat{z}_3)/\hat{r}_2 \quad (26a)$$

$$\sum \hat{F}_r = 0, \quad \hat{f}_{1r} = -(\hat{f}_{2r} + \hat{f}_{3r}) \quad (26b)$$

$$\sum \hat{F}_z = 0, \quad \hat{f}_{1z} = -(\hat{f}_{2z} + \hat{f}_{3z}) \quad (26c)$$

The orientations of the six components of nodal forces are expressed in the deformation coordinate system. They must be transformed into the global coordinate system. In addition, a forward rigid body rotation also must be imposed to the solid unit in fictitious state. Therefore,

$$\begin{Bmatrix} \tilde{f}_{Ir} \\ \tilde{f}_{Iz} \end{Bmatrix} = \mathbf{R}(+\Delta\theta) \mathbf{Q}^T \begin{Bmatrix} \hat{f}_{Ir} \\ \hat{f}_{Iz} \end{Bmatrix}, \quad I = 1, 2, 3 \quad (27)$$

Now the solid unit is back to t state. Finally, the contribution of circumferential stress σ_θ is considered. For simplicity, the distribution of σ_θ on the solid is assumed to be uniform and the nodal forces in r -direction are modified as

$$f_{Ir} = \tilde{f}_{Ir} + \frac{2}{3}\pi A_t \sigma_\theta, \quad I = 1, 2, 3 \quad (28)$$

where A_t denotes the area of solid unit at time t , and $\sigma_\theta = (\sigma_\theta)_a + \Delta\sigma_\theta$ is the circumferential stress.

4 von Mises Plasticity

In Eq. (27), the stress is calculated through a stress-strain relationship. In the numerical examples presented in Section 5, the material model of von Mises plasticity is used and briefly summarized here.

If the linear harden rule is used, then the uniaxial yielding stress can be expressed as

$$\sigma_y = \sigma_y^0 + \beta H \bar{\epsilon}_p \quad (29)$$

in which the symbols σ_y^0 , σ_y , H and $\bar{\epsilon}_p$ respectively denote initial yielding stress, subsequent yielding stress, plastic hardening modulus and effective plastic strain. The combination of isotropic and kinematic hardening can be achieved via introducing the parameter, β ($-1 < \beta \leq 1$). $\beta = 1$ and $\beta = 0$ respectively stand for isotropic and kinematic hardening rule.

In von Mises plasticity, the rate of deviatoric stress is calculated by the following relationship

$$\dot{\mathbf{S}} = 2\mathbf{G}\dot{\mathbf{e}}_e \quad (30)$$

where $\dot{\mathbf{e}}_e$ is the rate of elastic deviatoric strain, \mathbf{G} is the elastic shear modulus, and

$$\dot{\mathbf{e}}_e = \dot{\mathbf{e}} - \dot{\mathbf{e}}_p \quad (31)$$

$\dot{\mathbf{e}}$ is the rate of deviatoric strain. $\dot{\mathbf{e}}_p$ is the rate of plastic strain, which is normal to the yielding surface Φ and follows the flow rule,

$$\dot{\mathbf{e}}_p = \lambda \mathbf{n} \quad (32)$$

where λ is the proportionality constant, which can be determined using consistency condition. \mathbf{n} is the normal direction of the yielding surface.

$$\mathbf{n} = \frac{\partial\Phi}{\partial\xi} / \left| \frac{\partial\Phi}{\partial\xi} \right| \quad (33)$$

$$\Phi = \sqrt{\frac{3}{2} \boldsymbol{\xi} : \boldsymbol{\xi}} - \sigma_y = 0 \quad (34)$$

$\boldsymbol{\xi}$ is the effective stress defined by

$$\boldsymbol{\xi} = \mathbf{S} - \boldsymbol{\alpha} \quad (35)$$

$\boldsymbol{\alpha}$ is the back stress or the center of the yielding surface. In von Mises plasticity, it evolves using the rate form of

$$\dot{\boldsymbol{\alpha}} = \sqrt{\frac{2}{3}} (1 - \beta) H \dot{\epsilon}_p \mathbf{n} \quad (36)$$

Eqs. (30-36) completely define the stress-strain relationship of the material which deforms plastically. In this paper, the algorithm of radial return mapping [Krieg and Key (1976)] is used in the computer code to integrate the rate equations.

5 Numerical examples

In this section, four numerical examples are performed to demonstrate the accuracy and reliability of the approach proposed. A Fortran code VFIFE2D is used in these analyses.

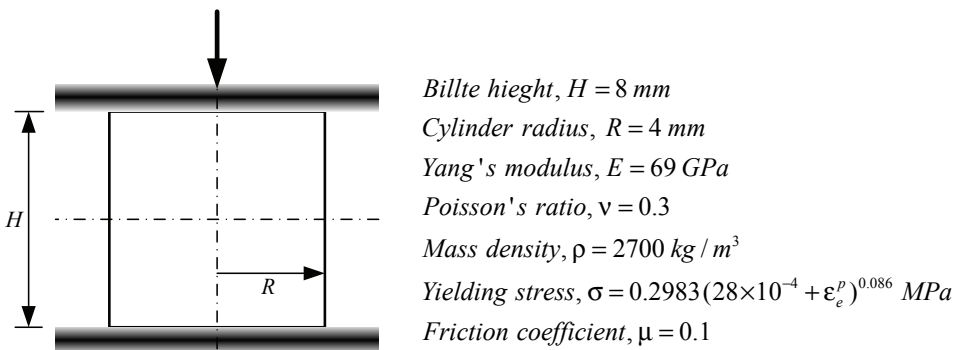


Figure 8: Cylindrical billet subjected to compression.

5.1 Example 1: Upsetting of a cylindrical billet

Figure 8 illustrates a cylindrical billet squeezed by two rigid plates for upsetting pre-form. The geometrical and material properties are specified in **Figure 8**. Only a quarter of model is analyzed for the double symmetric conditions. This example

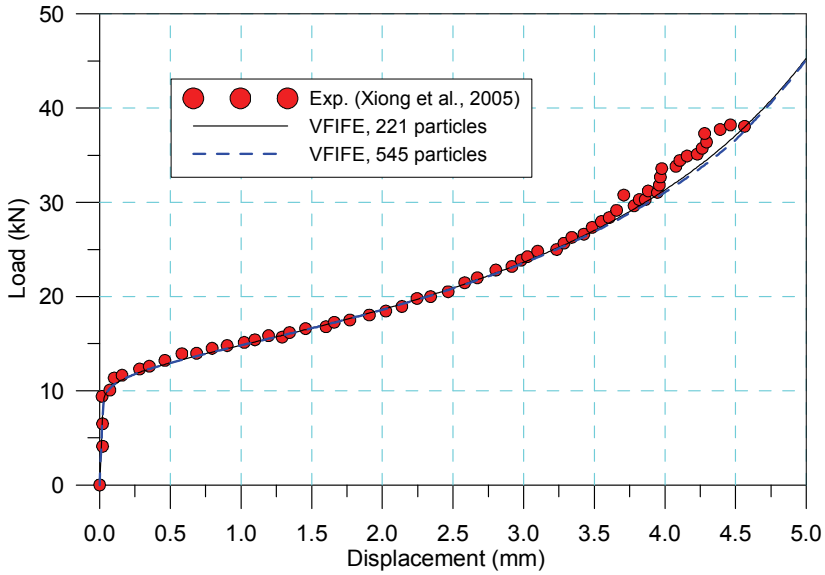


Figure 9: The curves of compressive load vs. displacement.

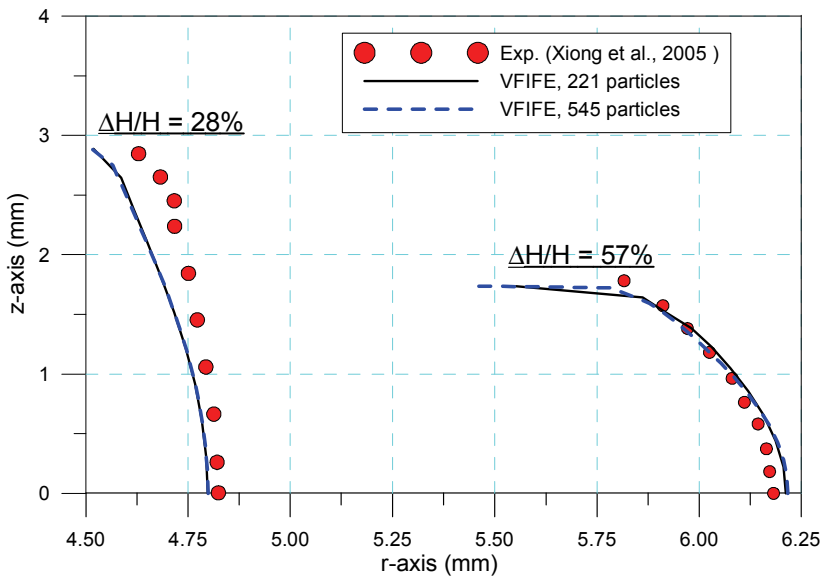
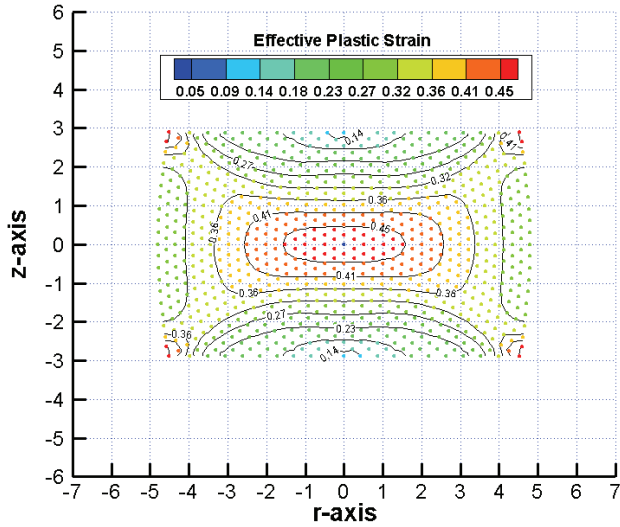
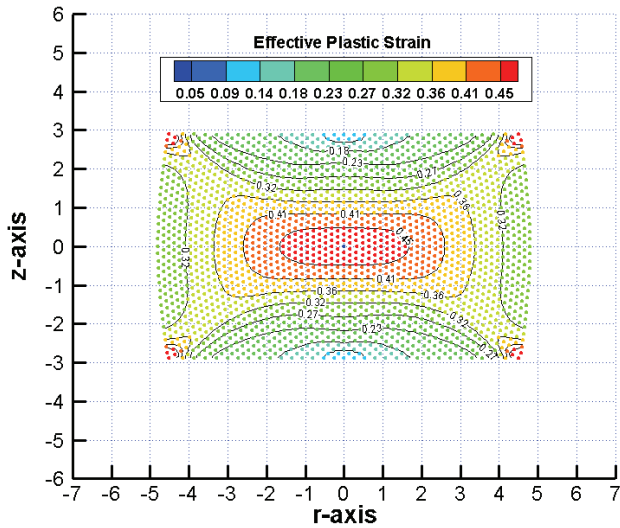


Figure 10: Geometrical profiles of the cross section of the billet under deformed stages 28% and 57% (ΔH : height change).

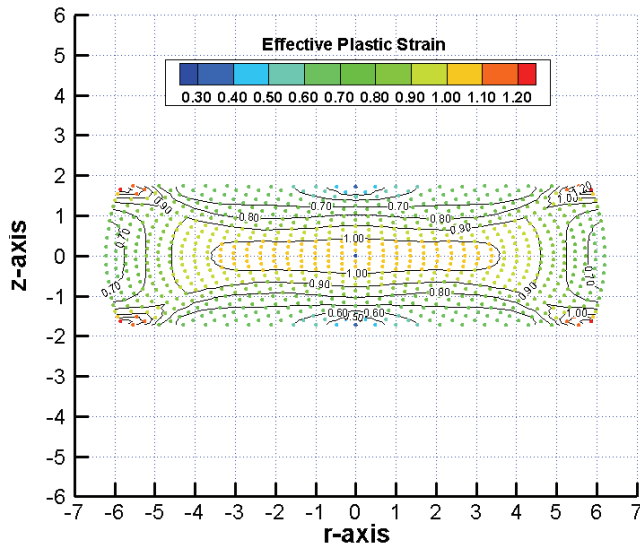


(a)

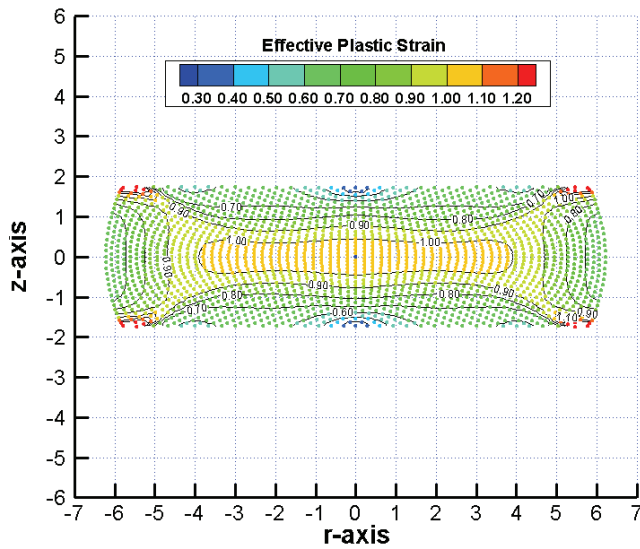


(b)

Figure 11: Contour plots of effective plastic strain as $\Delta H/H = 28\%$ (a) 221 particles (b) 545 particles.



(a)



(b)

Figure 12: Contour plots of effective plastic strain as $\Delta H/H = 57\%$ (a) 221 particles (b) 545 particles.

had been investigated by Xiong, Liu, Cao, Li, Rodrigues and Martines (2005) using experimental and numerical approaches. In this paper, two numerical models respectively with 221 and 545 particles are tested. The curves of compressive load versus displacement of the two models are plotted in **Figure 9**, and compared with the experimental result presented by Xiong, Liu, Cao, Li, Rodrigues and Martines (2005). It is obvious that both models show very good agreements with the experimental results. **Figure 10** plots the profiles of the deformed billet respectively when the ratio of height changes ($\Delta H/H$) of the billet is 27 % and 58 %. It reveals that the analysis results are comparable with those reported from experiment. **Figure 11** and **Figure 12** are the contour plots of effective plastic strain when the ratios of height change are 27 % and 58 %.

5.2 Example 2: Taylor bar impact analysis

This example considers the famous benchmark of the Taylor bar impact, as illustrated in **Figure 13**. The Taylor bar impact is frequently adopted in finite element community to test element performance on analyzing the metals undergoes large strain and plastic flow. The geometrical and material properties of the bar specimen are specified in **Figure 13**. In this example, three models respectively with 205, 427, and 729 particles are analyzed to investigate the deformed shapes of the bar at 0.08 ms.

Figure 14 shows the final shapes and the effective plastic strain distributions in the three models. The values of final length and mushroom sizes are listed in **Table 1** and compared with the results reported by Tran and Udaykumar (2004), and an analysis using commercial finite element code ABAQUS[®]/Explicit (2008). It can be found all the results of the three models show good agreements with those of ABAQUS[®] (2008) and Tran and Udaykumar (2004). None of so-called volumetric locking result [Zienkiewicz, Rojek, Taylor and Pastor (1998)] encountered in the analyses.

Table 1: The final length and mushroom radius.

	Final length (mm)	Final mushroom radius (mm)
VFIFE, 5x41 particles	21.55	7.077
VFIFE, 7x61 particles	21.54	7.084
VFIFE, 9x81 particles	21.49	7.133
Tran & Udaykumar (2003)	21.15	7.150
ABAQUS [®] CAX6M*	21.44	7.087

*1296 6-node triangular elements were used.

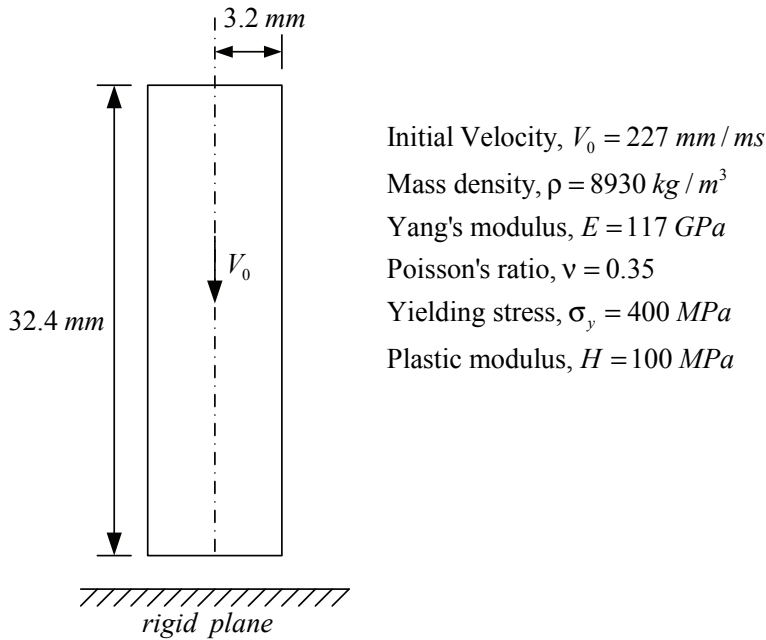


Figure 13: The Taylor bar impact test benchmark.

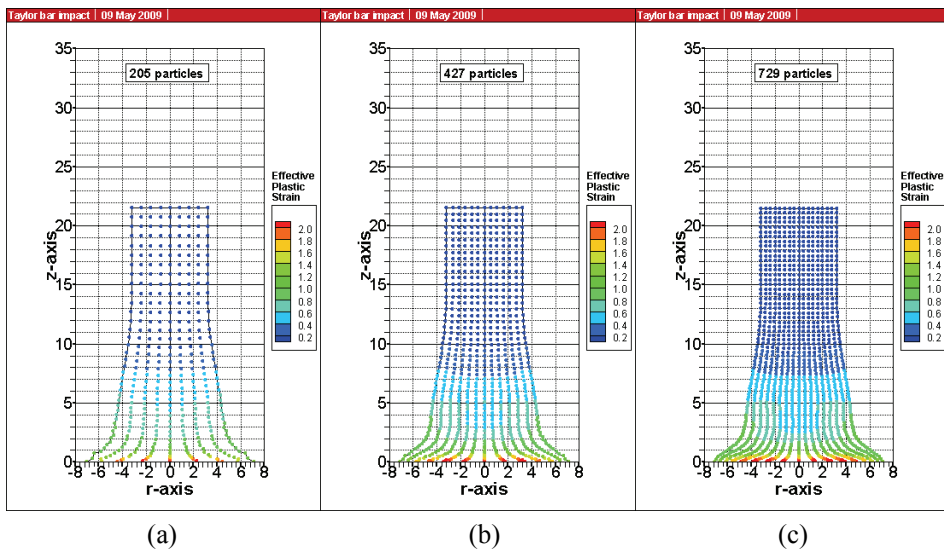
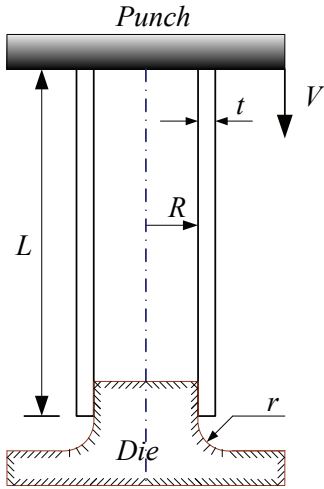


Figure 14: The final shape and effective plastic strain distributions of the models respectively with (a) 205 particles, (b) 427 particles and (c) 729 particles.



Length of tube, $L = 70 \text{ mm}$
 Internal radius of tube, $R = 18 \text{ mm}$
 Thickness of tube wall, $t = 2 \text{ mm}$
 Radius of die fillet, $r = 5 \text{ mm}$
 Mass density, $\rho = 2700 \text{ kg / m}^3$
 Yang's modulus, $E = 69 \text{ GPa}$
 Poisson's ratio, $\nu = 0.3$
 Yielding stress, $\sigma_y = 298.3(28 \times 10^{-4} + \epsilon_p)^{0.086} \text{ MPa}$
 Friction coefficient, $\mu = 0.1$

Figure 15: A single walled tube installed for external inversion.

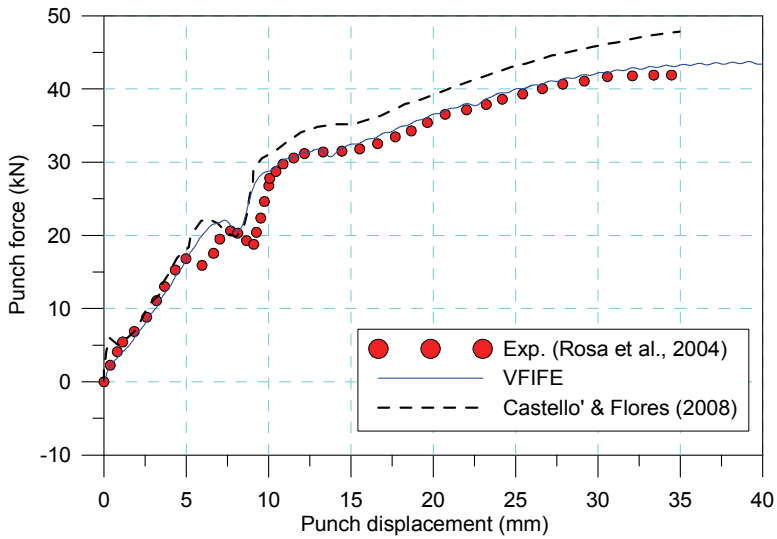


Figure 16: The force vs. displacement curves of punch.

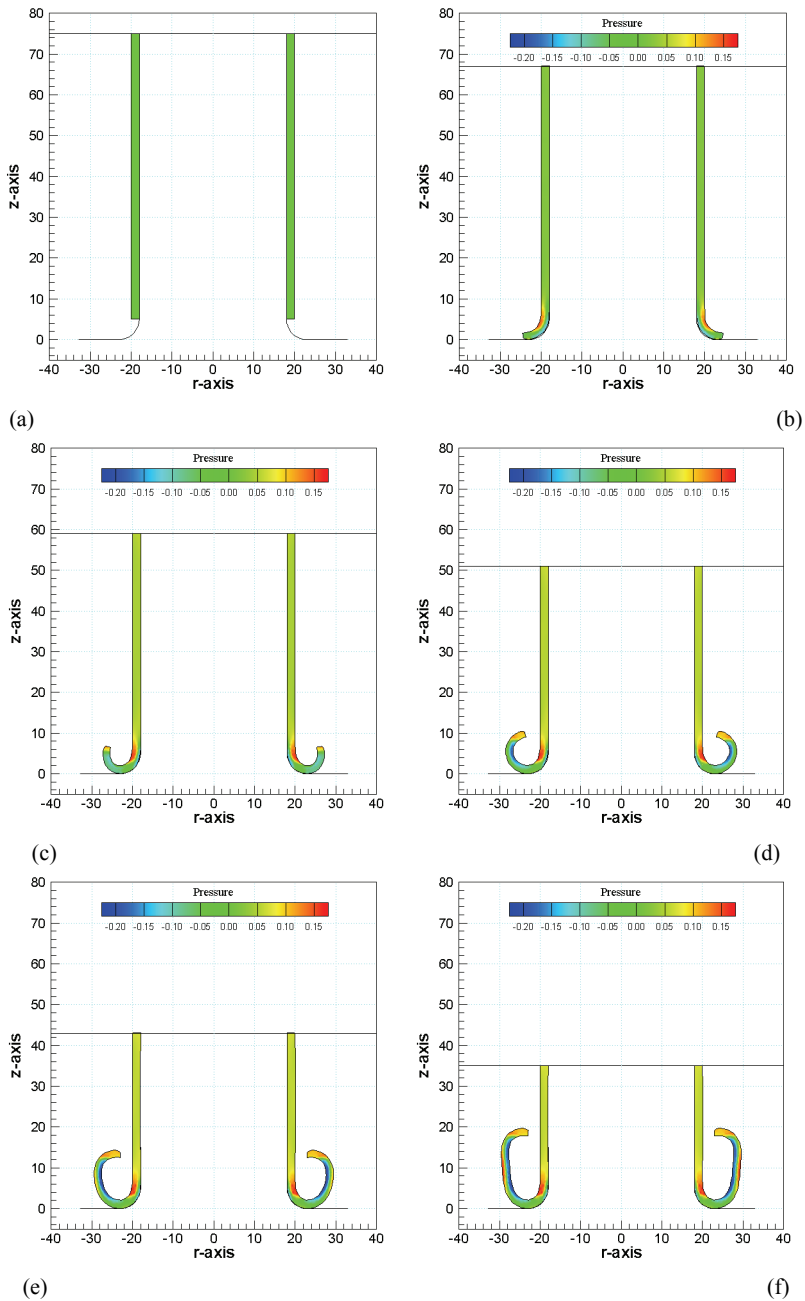


Figure 17: The configuration evolution of the inverted tube as punch displacements are (a) 0 mm (b) 8 mm (c) 16 mm, (d) 24 mm, (e) 32mm and (f) 40 mm.

5.3 Example 3: External inversion of a thin-walled tube using a die

This example considers a single walled tube installed on a die, and then subjected to a punch force applied at its top surface to form a double walled tube, as illustrated in **Figure 15**. This example was originally conducted by Rosa, Baptista, Rodrigues and Martins (2004) using experiments. Castelló and Flores (2008) took it to verify the accuracy of their work on axisymmetric solid element.

The geometric and material properties of the tube and die are specified in **Figure 15**. The Coulomb friction law is applied to treat the contact friction between the tube and die. The coefficient of friction is the same as that used by Castelló and Flores (2008), but the maximum frictional stress is limited to $\sigma_y/\sqrt{3}$. Totally 635 particles are used to construct the numerical model. The curve of punch load versus displacement is plotted in **Figure 16** and compared with the numerical results reported by Castelló and Flores (2008), and the experiment's conducted by Rosa, Baptista, Rodrigues and Martins (2004). It can be found that the result of VFIFE has good agreement with those presented by Castelló and Flores (2008), and Rosa et al. (2004). **Figure 17** shows the configuration evolution of the inverted tube.

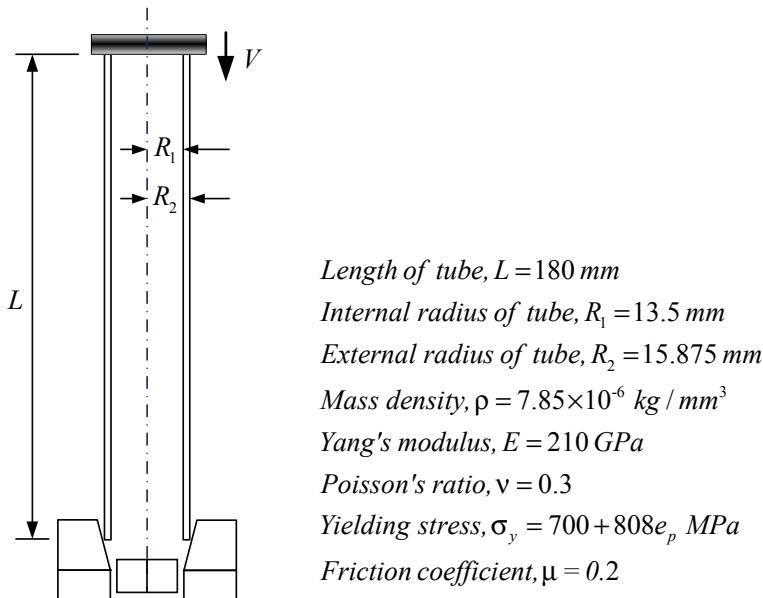
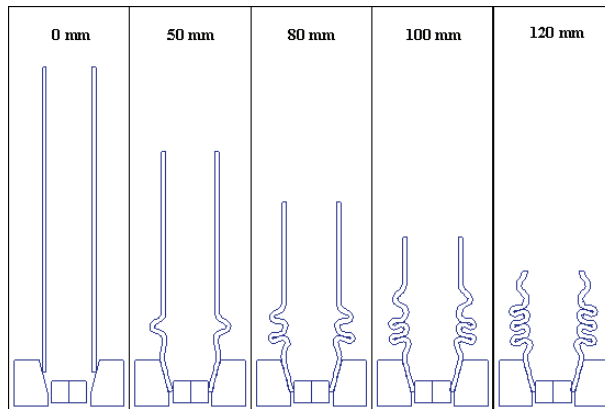
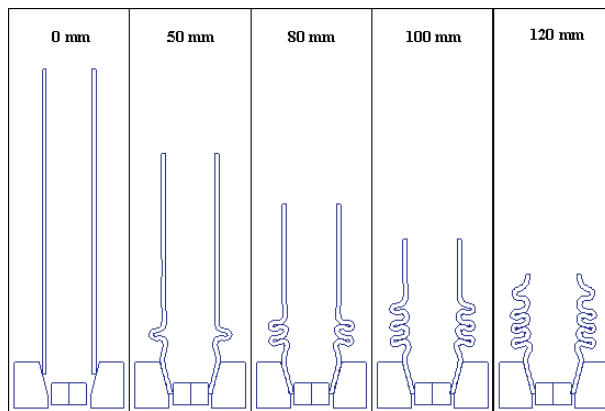


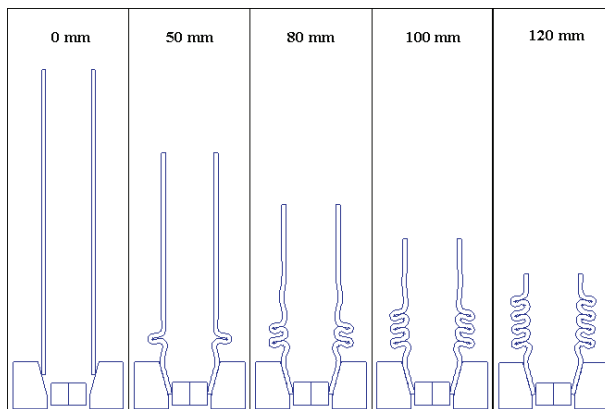
Figure 18: A tube installed on conical die for axial compression.



(a)



(b)



(c)

Figure 19: Progressive post-buckling of the tube respectively simulated by (a) 91x4 particles, (b) 106x4 particles, and (c) 121x4 particles.

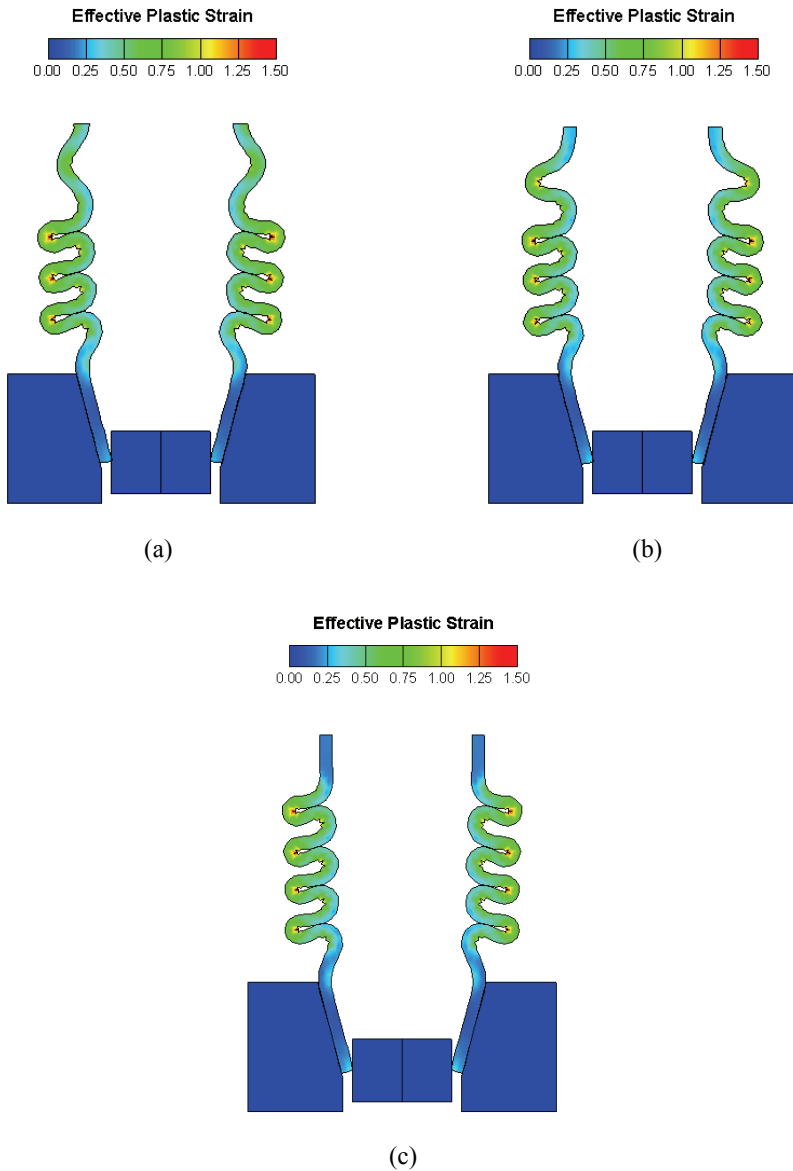


Figure 20: Effective plastic strain distribution as top surface displacement is 120 mm. (a) 91x4 particles, (b) 106x4 particles, (c) 121x4 particles.

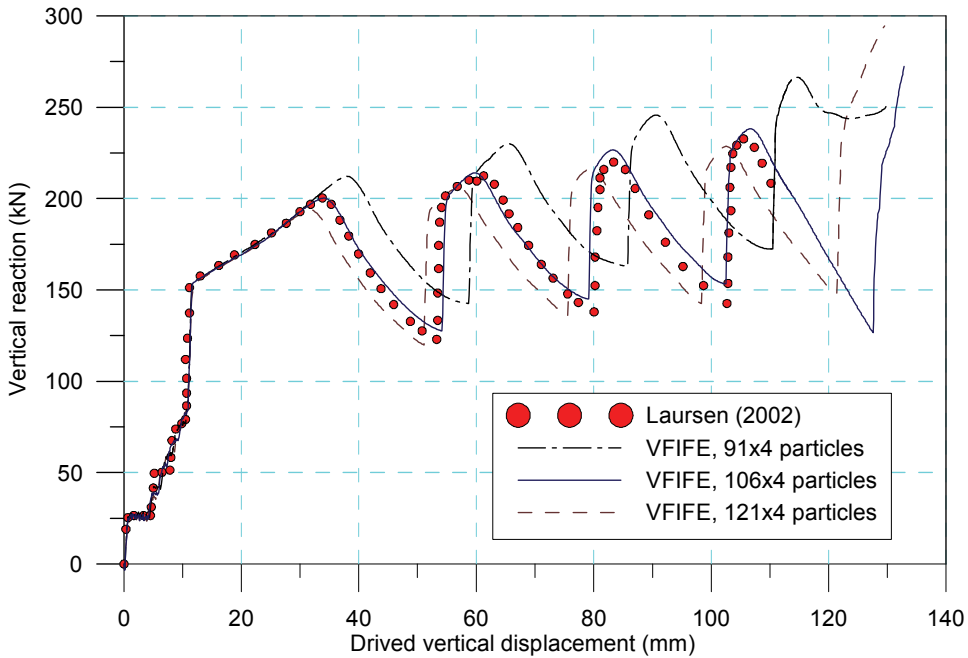


Figure 21: Curves of vertical reaction vs. top surface displacement.

5.4 Example 4: Progressive post-buckling of a tube

This example is taken from the textbook authored by Laursen (2002). Areias, César de Sá and Conceição António (2004) also had performed the same analysis to verify the accuracy of their contact algorithm. As shown in **Figure 18**, where a tube is installed on a die with conical inner shape, and subjected to an axial compression via slowly imposing downward velocity at its top surface. Under such condition, the tube can exhibit inelastic post-buckling and progressively form several wrinkles.

The geometric and material properties of the tube are specified in **Figure 18**. In this example, three models respectively with 91×4 , 106×4 , and 121×4 particles are tested. In addition, the penalty approach is used to impose contact forces when the contact between die and tube wall, and the self-contact of tube wall are detected.

Figure 19 shows the configurations of the tube evolving with the values of driven displacement. It can be found the discrepancy among the three models. **Figure 20** shows the buckling shapes and contour plots of effective plastic strain of each model when the displacement of top surface is 120 mm. **Figure 21** shows the curve of punch load versus displacement of VFIFE plotted together with the result reported by Laursen (2002) for comparison. Instead of the model with 121×4

particles, the result of the model with 106×4 particles has best agreement with that presented by Laursen (2002). In the work of Areias, César de Sá and Conceição António (2004), their curve is close to Laursen's (2002) but one more wrinkle forms. This is consistent with the result from the model analyzed using 121×4 particles.

6 Conclusions

In this paper, nonlinear analyses of axisymmetric solids with large deformation using vector mechanics have been presented. Instead of continuous functions, point value description is adopted to formulate the problem of solids. Analyses of numerical examples have also been conducted and performed using a code designed following the solution steps of vector form intrinsic finite element. They demonstrate that theory of vector form analysis is feasible. The solution procedures following the theory of vector form analysis are very simple. Algorithms are matrix-free and scalable. Therefore it is suitable for analyzing problems with complex properties and behaviors, such as fragmentation of reinforced concrete structures, which will be performed in subsequently published papers.

References

- Atluri, S.N.** (2004): *The Meshless Method (MLPG) for Domain & BIE Discretizations*, Tech Science Press.
- Atluri, S.N.** (2005): *Methods of Computer Modeling in Engineering & the Sciences*, Tech Science Press.
- ABAQUS®**, 2008. Manual Version 6.8, Simulia Inc.
- Areias, P. M. A.; César de Sá, J. M. A.; Conceição António, C. A.** (2004): Algorithms for the analysis of 3D finite strain contact problems. *Int. J. Numer. Meth. Engng.*, vol. 61, pp. 1107-1151.
- Castelló, W. B.; Flores, F. G.** (2008): A triangular finite element with local remeshing for the large strain analysis of axisymmetric solids. *Comput. Methods Appl. Mech. Engrg.*, vol. 198, pp. 332-343.
- Celigoj, C. C.** (2001): An improved assumed enhanced displacement gradient ring-element for finite deformation axisymmetric and torsional problems. *Int. J. Numer. Meth. Engng.*, vol. 50, pp. 899-918.
- Cundall, P. A.** (1971): A computer model for simulating progressive large scale movements in blocky rock systems. *Proc. Symp. Rock Fracture (ISRM)*, Nancy, vol. I, pp. 11-8.
- Krieg, R. D.; Key, S. W.** (1976): Implementation of a time dependent plasticity theory into structural computer programs. *Constitutive Equations in Visco-*

- plasticity: Computational and Engineering Aspects*, ASME, vol. 20, pp. 125-137.
- Laursen, T. A.** (2002): *Computational Contact and Impact Mechanics*, Springer-Verlag, Heidelberg.
- Rosa, P. A.; Baptista, R. M. O.; Rodrigues, J. M. C.; Martins, P. A. F.** (2004): An investigation on the external inversion of thin-walled tubes using a die. *Int. J. Plasticity*, vol. 20, pp. 1931-1946.
- Shi, G.** (1988): *Discontinuous Deformation analysis: a New Method for Computing Stress, Strain and Sliding of Block Systems*. PhD Thesis, Department Civil Engineering, University of California, Berkeley.
- Shi, C.; Wang, Y. K.; Ting, E. C.** (2004): Fundamentals of a vector form intrinsic finite element: Part III. Convected material frame and examples. *J. Mech.*, vol. 20, pp. 133-143.
- Ting, E. C.; Shi, C.; Wang, Y. K.** (2004): Fundamentals of a vector form intrinsic finite element: Part I. Basic procedure and a planar frame element. *J. Mech.*, vol. 20, pp. 113-122.
- Ting, E. C.; Shi, C.; Wang, Y. K.** (2004): Fundamentals of a vector form intrinsic finite element: Part II. Plane solid element. *J. Mech.*, vol. 20, pp. 123-132.
- Ting, E. C.; Wang, C. Y.; Wu, T. Y.; Wang, R. Z.; Chuang, C. C.** (2006): *Motion Analysis and Vector Form Intrinsic Finite Element*. Rept. No.: CBER-2006-W-001, NCU, Taiwan.
- Ting, E. C.; Duan, Y. F.; Wu, T. Y.** (2011): *Vector Mechanics of Structural Analysis*. Science press. (In Chinese).
- Tran, L. B.; Udaykumar, H. S.** (2004): A particle-level set-based sharp interface cartesian grid method for impact, penetration, and void collapse. *J. Comp. Physics*, vol. 193, pp. 469-510.
- Wu, T. Y.; Ting, E. C.** (2004): Vector form intrinsic finite element for 3D solids. *Proceedings of the 28th National Conference on Theoretical and Applied Mechanics*, Taipei (in Chinese).
- Wu, T. Y.; Wang, R. Z.; Wang, C. Y.** (2006): Large deflection and transient analysis of planar flexible frames. *J. Chinese Inst. Eng.*, vol. 29, pp. 593-606.
- Wu, T. Y.; Wang, C. Y.; Chuang, C. C.; Ting, E. C.** (2007): Motion analysis of 3D membrane structures by a vector form intrinsic finite element. *J. Chinese Inst. Eng.*, vol. 30, pp. 961-976.
- Wu, T. Y.; Ting, E. C.** (2008): Large deflection analysis of 3D membrane structures by a 4-node quadrilateral intrinsic element. *Thin-walled Struct.*, vol. 46, pp. 261-275.

Wu, T. Y.; Lee, J. J.; Ting, E. C. (2008): Motion analysis of structures (MAS) for flexible multibody system: planar motion of solids. *Multibody System Dynamics*, vol. 20, 3, pp. 197-221.

Wu, T. Y.; Tsai, W. C.; Lee, J. J. (2009): Dynamic elastic-plastic and large deflection analyses of frame structures using motion analysis of structures. *Thin-walled Struct.*, vol. 47, pp. 1177–1190.

Wu, T. Y.; Tsai, W. C.; Lee, J. J. (2010): In-plane Crushing Analysis of Cellular Materials Using Vector Form Intrinsic Finite Element. *CMC: Computers, Materials, and Continua*, vol. 17, pp. 175–214.

Xiong, S., Liu, W. K.; Cao, J.; Li, C. S.; Rodrigues, J. M. C; Martines, P. A. F. (2005): Simulation of bulk metal forming processes using the reproducing kernel particle method. *Computers & Structures*, vol. 83, pp. 547-587.

Zienkiewicz, O. C.; Rojek, J.; Taylor, R. L.; Pastor, M. (1998): Triangles and tetrahedral in explicit dynamic codes for solids. *Int. J. Num. Meth. Eng.*, vol. 43, pp. 565–583.